# Computer Simulations of Nucleation of Nanoparticle Superclusters from Solution

Siddique J. Khan, C. M. Sorensen, and A. Chakrabarti*

Department of Physics, Kansas State University, Manhattan, Kansas 66503, United States

ABSTRACT: This paper presents simulation studies of nanoparticle supercluster (NPSC) nucleation from a temperature quenched system. The nanoparticles are represented as 5 nm, spherical gold nanoparticles ligated with alkane thiols. The pair potential accounts for the van der Waals interaction between the metallic cores and ligand−ligand and ligand−solvent interactions. Phenomena well-known for molecular systems are observed including a prenucleation induction period, fluctuating prenucleation clusters that predominately add monomers one at a time, a critical nucleus size, and growth of NPSCs from solution in the presence of an equilibrium supernatant, all consistent with classical nucleation theory. However, only the largest prenucleating clusters are dense, and the cluster size can occasionally range greater than the critical size in the prenucleation regime until a cluster with low enough energy occurs, then nucleation ensues. Late in the nucleation process, the clusters display a crystalline structure that is a random mix of face-centered cubic (fcc) and hexagonal close-packed (hcp) lattices and indistinguishable from a randomized icosahedra structure.
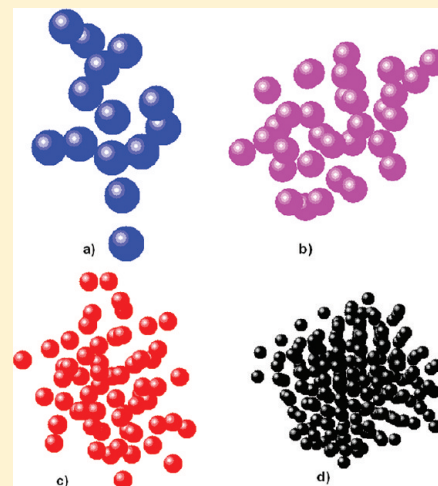
I. INTRODUCTION

Nucleation of one phase of matter from another is of great and enduring interest. Applications range from materials processing, including both atomic- and molecular-based materials and the new nanomaterials, to particle formation in the atmosphere with consequences for the global environment. Nucleation in nanomaterials is of particular interest, as recent advances in synthetic chemistry have given rise to a wide variety of nanoparticles (NPs) with a high degree of both chemical and physical uniformity. These uniform NPs (also called nano-clusters of atoms) serve as the atoms and molecules of a new class of NP-based materials.[1−4] Since NPs and their clusters are easily seen by table-top laboratory methods such as light scattering, NP solution nucleation provides an experimentally accessible system that will reflect on the age-old problem of atomic and molecular system nucleation.

Nanoparticles are usually surface ligated with any of a variety of organic compounds, and these ligands cause colloids of the NPs to be stable against irreversible aggregation. Often these colloids act as solutions with the NPs displaying reversible temperature and solvent-dependent solubility. In many cases when the NPs are highly uniform, the precipitating solid is a two- or three-dimensional superlattice of the NPs.[5,6] Thus there is strong analogy to the phase behavior of molecular solutions, and it is then reasonable to ask what controls the phase behavior of NP solutions and what is the nature of the nucleation and growth[7−15] into superclusters of NPs (often NPs are referred to as "nanoclusters", so we use the term "supercluster" (SC) to imply a cluster of NPs, i.e., NPSCs)? Does the classical nucleation theory (CNT) apply to NP

solution nucleation or is the pathway more complex? Does the two-step model proposed for protein crystallization[16−18] (where a stable cluster forms as a dense liquid as the first step and then the particles in the cluster reorganize into an ordered structure) apply to NPs? What is the shape of the fluctuating prenucleating NPSCs? Are these spherical as assumed in classical nucleation theory, or do they have other shapes as implied by recent colloid work?[19,20] Such questions are not only of inherent intellectual interest but are also very useful, for with an understanding of this science, we will be able to control the self-assembly of NPs into either superlattices, ramified aggregates, gels, or films on surfaces.

Once a system is quenched from a stable to a metastable regime, nucleation phenomena divide into two halves: those that happen before a critical nucleus occurs, and those that happen after the critical nucleus forms. Before the critical nucleus forms, we desire to know the size, structure and number of prenucleation NPSCs that appear and disappear in the system. After the critical nucleus forms, we desire to know the kinetics of the ensuing cluster growth, number density, and structure. Although a few experiments exist in the literature on NPSC nucleation,[9,15] theoretical work is rare.

In this paper we present a comprehensive theoretical study of NP solution nucleation. The NP pair potential is a recently developed phenomenological model[20] for the effective interaction potential between two ligated gold nanoparticles.

In our phenomenological model, we consider a solution of gold nanoparticles with various alkane-thiol ligands in toluene. Ligands are considered as flexible chains and free-energy of mixing, and elastic contributions to the free-energy due to ligand compressions are considered in addition to van der Waals interactions. In general, our results support the application of classical nucleation theory to the NPSC nucleation. We find, however, interesting details that are applicable to both NP and molecular solutions that extend and improve our understanding of nucleation phenomena.

II. MODEL AND SIMULATION METHOD

A detailed description of our phenomenological model has been presented in ref 20. Here we summarize the main components of the interaction potential. The van der Waals interaction potential between two spherical particles in the pairwise summing approximation can be written as

$$V_1 = -\frac{A}{12}\left[\frac{1}{x^2-1} + \frac{1}{x^2} + 2\ln\left(1 - \frac{1}{x^2}\right)\right] \quad (1)$$

Here, A is the effective Hamaker constant, and x is the scaled center−center distance between the two particles, i.e., $x = r/\sigma$, where r is the center−center distance and σ is the diameter of the gold core. In the presence of ligands on the nanoparticles, the effective Hamaker constant between two nanoparticles will have contributions from the bare gold−gold Hamaker constant, the ligand−ligand Hamaker constant (treated as a continuum layer), and the solvent−solvent Hamaker constants. The effective Hamaker constant between two ligated nanoparticles can be estimated and is taken as 75.5 kT in our calculations (with $T = 300\ K$) as used in a previous study.[21]

To estimate the free-energy of mixing of the ligands when ligand layers from two different nanoparticles start overlapping, one needs to consider two different regimes. In the first regime, the ligand chains undergo interpenetration, and in the second regime the chains undergo interpenetration and compression. Free-energy of mixing in both regimes I and II is known in the literature[22] in terms of the Flory χ-parameter between the solvent and the flexible tethered chains. In terms of our rescaled variables, one can write this in regime I as

$$\frac{V_2}{kT} = \frac{\pi\sigma^3}{2v_m}\phi_{av}^2\left(\frac{1}{2} - \chi\right)[x - (1 + 2\tilde{L})]^2;$$

$$1 + \tilde{L} < x < 1 + 2\tilde{L} \quad (2)$$

In our notation, the length of the ligands is denoted by L, while $\tilde{L}$ is the scaled length of the ligand chains, i.e., $\tilde{L} = L/\sigma$; v_m is the volume of a solvent (toluene) molecule, and ϕ_{av} is the average volume fraction of the ligand segments in the tethered layer, assumed to have a step profile with a uniform segment density in the layer and a sharp drop to zero segment density outside of the layer. Similarly in regime II, the free-energy of mixing can be written as

$$\frac{V_3}{kT} = \frac{\pi\sigma^3}{v_m}\phi_{av}^2\left(\frac{1}{2} - \chi\right)\tilde{L}^2\left[3\ln\left(\frac{\tilde{L}}{x-1}\right) + 2\left(\frac{x-1}{\tilde{L}}\right) - \frac{3}{2}\right];$$

$$x < 1 + \tilde{L} \quad (3)$$

An elastic contribution to the potential due to ligand compression is also present in region II and is known in the literature.[23] On close approach between two nanoparticles, the volume available for the tethered chains to fit is much less than

when the two nanoparticles are infinitely separated. This gives rise to a loss of configurational entropy of the tethered chains and leads to an elastic repulsion between two nanoparticles. In terms of the scaled variables, this can be written as

$$\frac{V_4}{kT} = \pi\nu\sigma^2\left[(x-1)\left(\ln\frac{x-1}{\tilde{L}} - 1\right) + \tilde{L}\right]; \quad x < 1 + \tilde{L} \quad (4)$$

where ν is the number of ligands per unit area of the nanoparticle.

The total effective pair potential between two nanoparticles in toluene is the sum of all four contributions listed in eqs 1−4 and is denoted as $V(x)/kT$. This effective pair potential with decanethiol (C10), dodecanethiol (C12), and hexadecanethiol (C16) ligands, respectively, is shown in Figure 1 and is used in
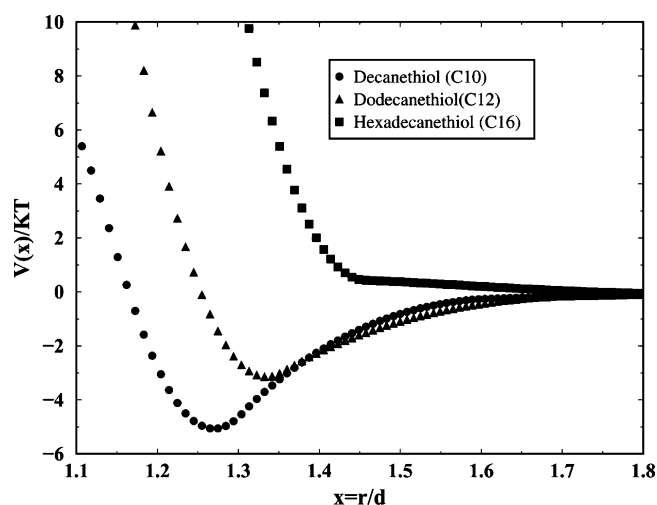

Figure 1. Effective pair potential between two nanoparticles in toluene with decanethiol (C10), dodecanethiol (C12), and hexadecanethiol (C16) ligands.

our Brownian dynamics (BD) study. The location of the minimum of the potential in each case compares extremely well to the superlattice constant measured in experiments.[2]

The equations of motion for the BD simulation read as

$$\ddot{\vec{r}}_i = -\vec{\nabla}U_i - \Gamma\dot{\vec{r}}_i + \vec{W}_i(t) \quad (5)$$

where Γ is the friction coefficient and W_i, the random force acting on each colloidal particle i, is a Gaussian white noise satisfying a fluctuation−dissipation relation. The potential U is modeled as an effective pair-potential shown in Figure 1, i.e., a mixture of van der Waals, ligand mixing, and elastic terms as discussed earlier. We consider three-dimensional systems of size $L = 128\ \sigma$ in units of monomer diameter σ. We have performed several runs for $L = 64\ \sigma$ as well. All other length scales are measured in units of σ as well. We consider a range of monomer volume fractions from $f = 0.0023$ to 0.0038, with the number of monomers ranging up to $N_m = 16\ 000$. Results presented here are based on the analysis of the C12 system.

We choose $\Gamma = 0.5$ and time step $\Delta t = 0.005$ in reduced time units of $\sigma(m/kT)^{1/2}$ with $m = 1$. For this choice of Γ, particle motion is purely diffusive for $t \gg 1/\Gamma$, i.e., $t \gg 2$ in our units. Periodic boundary conditions are enforced to minimize wall effects. All simulations start from a random initial monomer conformation, and the results for the nucleation study are averaged over several (10−20) runs. We note that motions of

ligated nanoparticles can be affected by shearing force produced by other particles nearby due to the existence of ligands beside the pair potential described in Figure 1. This effect is not considerd in our work. However, as these simulations are performed at low volume fractions (i.e., $f = 0.0023-0.0038$,) we expect that the shearing effect due to the presence of other particles is weak.

III. RESULTS

We first compute the number of unaggregated monomers, N_m, left in the system a long time after quenching the system with a given volume fraction. From this (see Figure 2), the saturation
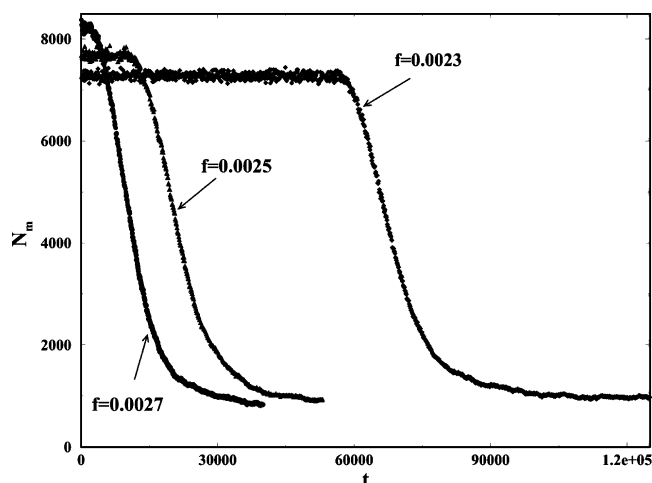

Figure 2. Variation of number of unaggregated monomers left in the system (N_m) as a function of time after a quench at zero time for the volume fractions of $f = 0.0027$, 0.0025, and 0.0023 as indicated by arrows. The equilibrium volume fraction of unaggregated monomers is estimated as $f_e = 0.0002$ in all three cases.

region at late times where N_m is constant with time indicates an equilibrium volume fraction f_e of 2×10^{-4}. At early times, the constant value of unaggregated monomers, N_m, indicates a region of metastability of the solid phase in which small, prenucleation NPSCs appear and disappear in the system.

Next, we choose an unaggregated monomer volume fraction f, larger than the equilibrium value f_e. For our choices of f, only a few (in many cases, we find only one cluster growing) isolated solid NPSCs nucleate and grow after some induction time. Snapshots of such a growing NPSC amidst the colloidal gas phase are shown in Figure 3 at various times along with a zoomed-in version of the NPSC at the latest time.

III.A. Application of CNT. According to CNT, the free-energy ΔG required to form a homogeneous cluster of N particles is governed by two competing factors: the bulk interaction energy and the surface energy of the cluster. Thus one can write

$$\Delta G = -N\Delta\mu + 4\pi\gamma r^2 \tag{6}$$

where N is the number of particles in the cluster, r is the radius of the cluster, and γ represents the surface energy of cluster/gas interface.[24,25] $\Delta\mu$ represents the difference in chemical potential between the two phases. This expression is valid for the case of condensed cluster phase with the assumption that the cluster is spherical (see ref 24 for details).
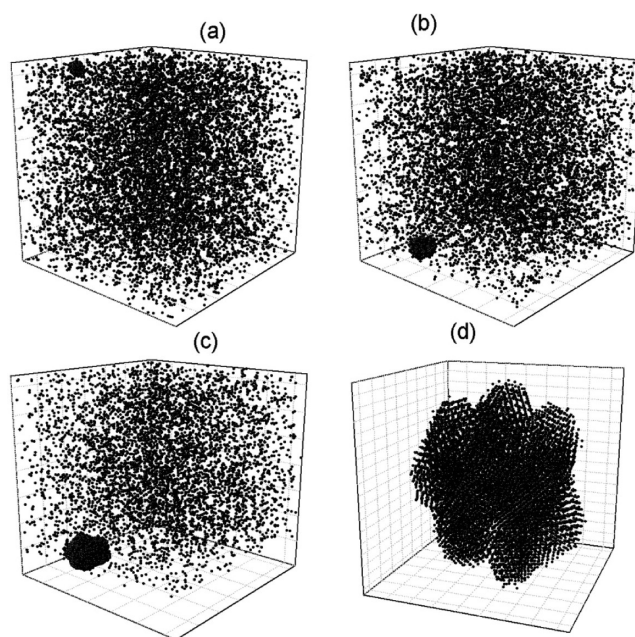

Figure 3. Time evolution of a quenched NP system showing a single NPSC growing in the system (a) at $t = 3000$, (b) at time $t = 5000$, and (c) at time $t = 10\,000$. (d) Magnified nucleating NPSC of the system at $t = 40\,000$. The volume fraction in this case is $f = 0.0027$.

Equation 6 can also be written as

$$\Delta G = \frac{-4\pi r^3 \Delta\mu}{3v_0} + 4\pi\gamma r^2 \tag{7}$$

where v_0 is the volume of each particle. The minimum separation of the particles in the nucleating NPSC coincides with the minima of total interaction potential between the nanoparticles, which is 1.33σ for the case of C12. Thus, we considered the effective volume of the nucleating NPSC as $v'_0 = \pi\sigma'^3/6$, where $\sigma' = 1.33\sigma$.[26]

Minimizing ΔG with respect to r gives the critical radius (r^*) and cluster size N^* required to form a nucleating cluster. These are given by

$$r^* = \frac{2\gamma v'_0}{\Delta\mu} \tag{8a}$$

and

$$N^* = \frac{32\pi\gamma^3 v'^2_0}{3(\Delta\mu)^3} \tag{8b}$$

According to CNT, clusters containing particles less than N^* shrink and dissolve back in the gas phase, while clusters with number of particles greater than N^* grow spontaneously by the addition of monomers or smaller clusters present in the system.[27] Note that the interfacial tension is a very sensitive term in all equations.

The change in chemical potential during the condensation/sublimation of the solute molecules in a solution is given by

$$\Delta\mu = kT \ln\left(\frac{a}{a_e}\right) \tag{9a}$$

where a and a_e are the chemical activity of the solute molecules at the volume fractions f and f_e, respectively. For low volume

fractions, (i.e., dilute systems), one can replace activity by the volume fraction of the solute molecules (for details, see ref 27).

$$\Delta\mu(f, T) = kT \ln\left(\frac{f}{f_e(T)}\right) = kT \ln(S) \tag{9b}$$

where S is called the *supersaturation* of the system. Equations 8a and 8b can be written in terms of S as

$$r^* = \frac{2\gamma v'_0}{kT \ln(S)} \tag{10a}$$

and

$$N^* = \frac{32\pi\gamma^3 v'^2_0}{3(kT \ln(S))^3} \tag{10b}$$

Substituting eqs 10a and 10b into eq 7, one can obtain the activation barrier energy ΔG^* required to initiate nucleation as

$$\Delta G^* = \frac{16\pi v'^0_2 \gamma^3}{3(kT \ln S)^2} \tag{11}$$

The induction time t_{ind} can be defined as the time elapsed between the creation of supersaturation and formation of nuclei of critical size.[27,28] To determine the value of induction time in our simulations, we studied the variation of the mean coordination number (i.e., the mean number of neighbors) $C_n(t)$, for particles with at least one neighbor.[29] Figure 4 shows
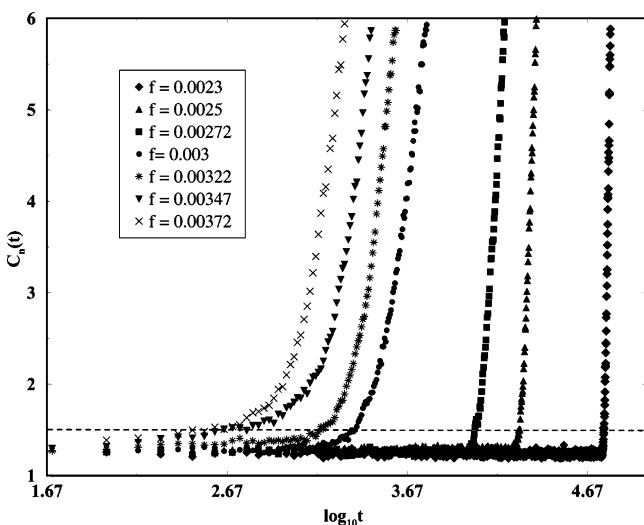

Figure 4. A plot of the monomer mean coordination number $C_n(t)$ as a function of time after quench. The dashed line at $C_n(t) = 1.5$ is our criterion to indicate nucleation with which the induction time can be determined.

the variation of the mean coordination number as a function of time for the system in one simulation run for various values of supersaturation. As shown in Figure 4, $C_n(t)$ remains constant at a small value over a certain period of time, and then there is a sudden rise in $C_n(t)$ indicating the formation of a critical nucleus.[34] Choosing a particular value of $C_n(t)$ helps to determine the induction time. We have somewhat arbitrarily chosen $C_n(t) = 1.5$ as the threshold for nucleation to determine induction time t_{ind}. However, we have tested that the other reasonable choice of $C_n(t)$ as the threshold value does not affect

the calculation below for the interfacial tension or the critical size.

The nucleation rate or the nucleation frequency J is related to the activation barrier energy ΔG^* by the relation[28]

$$J = J_0 \exp\left(\frac{-\Delta G^*}{kT}\right) \tag{12}$$

The induction time is inversely related to the nucleation frequency,[30]

$$t_{ind} = C \exp\left(\frac{\Delta G^*}{kT}\right) \tag{13a}$$

Thus, using eq 11, we can write

$$t_{ind} = C \exp\left(\frac{16\pi v'^0_2 \gamma^3}{3kT(kT \ln S)^2}\right) \tag{13b}$$

The veracity of eq 13b for our simulation is seen in Figure 5, where $\ln(t_{ind})$ is plotted versus $1/(\ln S)^2$. According to eq 13b,
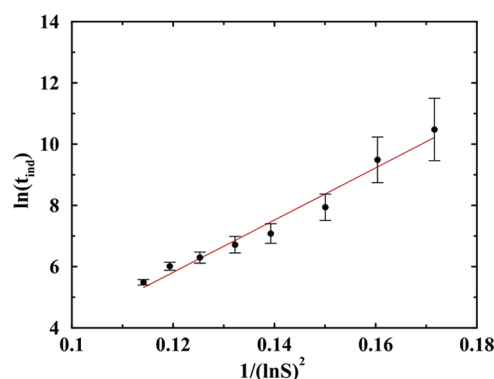

Figure 5. Plot of the induction time versus supersaturation S. The induction time is averaged over 10 different initial configurations for each S value.

such a plot should be linear, and that is found to be the case. From the slope of the graph in Figure 5, the interfacial tension γ is found to be $\gamma = 1.3 \pm 0.05 kT/\sigma'^2$. This is about twice the value of $\gamma = 0.6 kT/\sigma^2$ expected for a face-centered cubic (fcc) close-packed lattice based on entropic considerations[8] so the result is gratifying because it properly accounts for the size of the NP, which is 1.5 orders of magnitude larger than the atomic and molecular length scales. The value of γ is also about twice the experimental value of $0.76\ kT/\sigma^2$ obtained in ref 9 from a study of gold NPSCs nucleating from a *different mixed solvent* of toluene−butadiene. Given the inaccuracies in our theoretical model and the errors involved in estimating γ from a simulation of a finite-sized system, such a discrepancy is not unexpected. Using the simulation value of γ in eq 10b, we obtain that the critical value of the size of the nucleating NPSC is $N^* \approx 10$ (see Table 1).

III.B. NPSC Dynamics. The dynamics of the biggest NPSC can be divided into two regions, as shown in Figure 6. The region where the nucleating cluster is unstable and fluctuates around an average size $N = 10$, indicated by the hatched area, is named as the *prenucleating regime*, and the region where a nucleating cluster smoothly grows to a stable size is named as *nucleating regime*. In order to understand the mechanism of nucleation, we examined the fluctuations in size by looking at the absolute value of the change in size of the biggest cluster

Table 1. Comparison of the Calculated Values of the Critical Size n^* at Different Supersaturation Values S for CNT and the Fisher Droplet Model

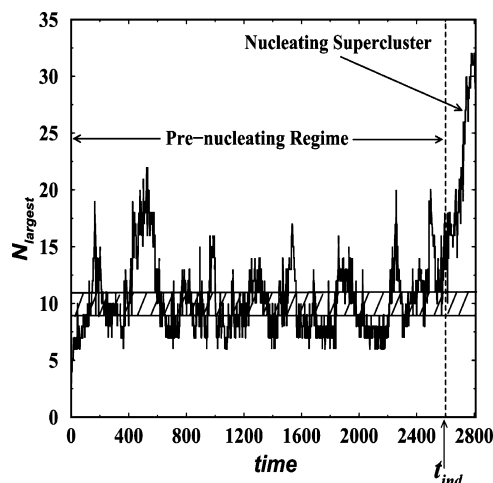| S	S1 10.95	S2 11.9	S3 12.95	S4 14.28	S5 15.333	S6 16.52
N^*(CNT)	9.5	8.5	7.5	6.75	6.25	5.75
N^*(Fisher Model)	12	11.2	10.3	9.5	8.3	7.4

Figure 6. Plot showing the size fluctuations of the biggest NPSC in the prenucleation regime. The induction time is ∼2600. Excursions above the critical size of $N^* \approx 10$ (cross hatched region) can be observed in the prenucleation regime.

(ΔN) between two successive time steps. A distribution of ΔN, averaged over 50 runs, is shown in Figure 7 in a log–linear plot during the growth and fragmentation of the biggest cluster. Figure 7 shows that both prenucleating and nucleating regimes are similar and are dominated by the exchange of monomers and dimers. A slope is drawn as a guide to show the exponential
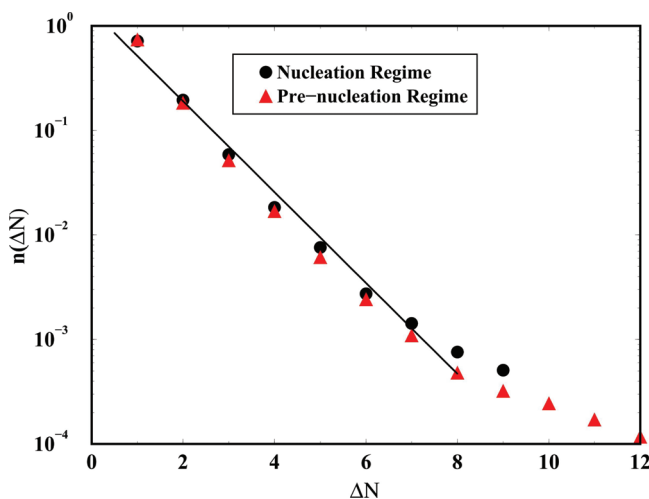

Figure 7. A log–linear plot of the normalized distribution of the absolute value of the change in size of the biggest NPSC ΔN during consecutive time steps for both prenucleation and nucleating regimes. A slope is drawn as a guide to show the exponential behavior of the distribution, which seems to describe the data well for smaller values of ΔN. Larger ΔN occurrences are rare and thus have much larger uncertainty.

behavior of the distribution, which seems to describe the data well for smaller values of ΔN. Larger ΔN occurrences are rare and thus have much larger uncertainty. The dominance of the addition/removal of monomers in both regimes is consistent with the CNT.

Another important feature observed in Figure 6 are the excursions in the size of the biggest cluster in the prenucleating region, leading to the formation of unstable clusters of size up to $N \approx 20$ in some cases; a size far greater than the critical nucleus size predicted by CNT (i.e., $N \approx 10$). These excursions indicate the formation and break-up of the biggest cluster in the system. To understand these excursions, we compared the energy per NP between prenucleation and nucleation regime clusters. This comparison is shown in Figure 8, where we can
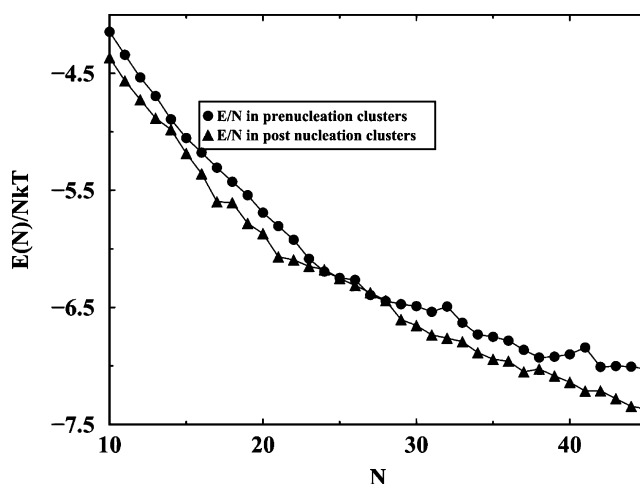

Figure 8. Plot of the energy per nanoparticle of the prenucleation and nucleation NPSC as a function of the NPSC size N.

see that the nucleating NPSC's have lower energy than the prenucleation clusters at any given size of the nucleating NPSC. This implies that the prenucleating cluster fluctuates around the critical size predicted by CNT until a NPSC of enough lower energy appears in the system and grows to a stable size.

III.C. Morphology and Shape of Prenucleating NPSCs. Next, we studied the morphology of the biggest NPSC in both prenucleating and nucleation regimes. At early time (i.e., in prenucleating regime), the biggest NPSC appears to be noncompact (see Figure 9a), whereas at late times (i.e., in nucleation regime), the structure of the NPSC appears to be more compact (Figure 9b,c,d). As CNT assumes that nucleating clusters are compact and spherical in shape, we further address the issue of shape by plotting the number of monomers in the prenucleating NPSCs as a function of the NPSC radius of gyration, R_g, for both the largest NPSC in the system and all NPSC of specific sizes. The analysis for the biggest NPSC is averaged over 50 runs. We have also included in this figure *artificially* created clusters of relevant sizes randomly placed on the lattice sites of pure fcc and body-centered cubic (bcc) crystals using the self-avoiding random walk method. Figure 10 shows the R_g versus N plot for the biggest NPSC in the system in the prenucleation regime along with other small NPSCs present in the system at a given time. It is evident that all small NPSCs are well described by self-avoiding walks on an fcc lattice. No evidence of any bcc structure in the prenucleating NPSCs is seen, although such theoretical claims exist in the literature.[31,32] It is quite possible
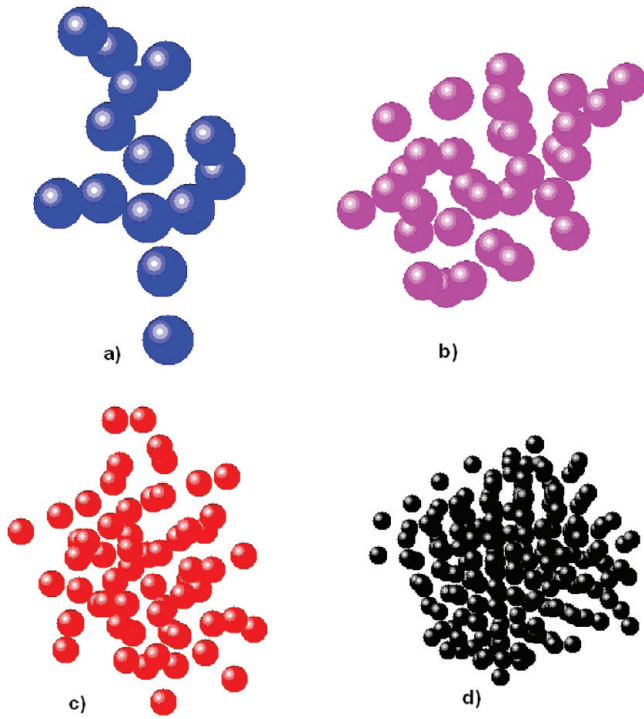
Figure 9. Pictures of the biggest NPSC in the system at various times after quench: (a) $t = 2000$ with $N = 14$, (b) $t = 3000$ with $N = 33$, (c) $t = 4000$ with $N = 60$, and (d) $t = 5000$ with $N = 209$. The nucleation induction time that separates the pre- and postnucleation regimes is $t \approx 2800$. The symbol sizes for monomers are scaled so that each cluster appears to have the same linear size.
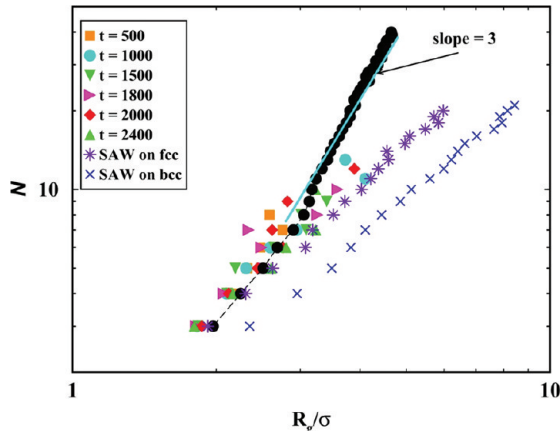

Figure 10. Plot of the number of NPs in the NPSC versus supercluster radius of gyration for: 1) the largest NPSC (Nlargest ($\bullet$)) at various times in the system and 2) the other, smaller NPSCs in the system at prenucleating times.

that the formation of a bcc nucleating phase depends on the amount of supercooling, and a detailed study is needed to sort out this issue. We also note that some experimental evidence of bcc−fcc transition is seen in charged colloidal systems.[33,34] In the charged colloidal system, however, the bcc phase is a stable, equilibrium phase for low volume fractions unlike in the NP systems considerd here. It is not clear at this point whether this makes a difference in the nucleation of the bcc phase.

We further note that the largest NPSC in the prenucleating system has a compact morphology once bigger than about size $N = 10$, the critical size. Since the largest cluster plays a major

role in nucleation, the compact morphology for a size comparable to N^* again supports the CNT scenario.

III.D. Application of the Fisher Droplet Model Theory. Although the nucleation of our NPSCs is reasonably well described by CNT, we further analyzed the energetics of the nucleation process going beyond the CNT. Such a theoretical development exists in the literature in terms of Fisher's droplet model, which differs from the CNT by an additional contribution to the total free energy to accommodate the entropic effects of the shape of the clusters. According to this model, the free energy required to form a nucleating cluster is given by

$$\Delta G = \frac{-4\pi r^3 \Delta \mu}{3 v'_0} + 4\pi \gamma r^2 + \tau kT \ln\left(\frac{4\pi r^3}{3 v'_0}\right) \tag{14}$$

where the logarithmic term on the right-hand side is due to the statistical mechanical treatment of the free energy, which includes contributions from the translational, rotational, and configurational partition functions. Lothe and Pound[35] included the translational and rotational degrees of freedom of the cluster. According to their theory, $\tau = -4$. Fisher obtained τ to be 2.2 arising from configurational entropy contributions.[36,37] Other modifications of this model were carried out by several groups. For example, Reiss, Katz, and Cohen included the center of mass fluctuations, and Reiss assumed the nucleating droplet to be a liquid drop and made appropriate modifications. Fisher's theory is found to be in good agreement with experimental results.[38−40] Later, further modifications were proposed by Lowe and Wallace to account for the presence of smaller clusters in the system,[41] and they argued that $\tau = 1.25$ works best to explain experimental data. We have used a modified Fisher droplet model and used τ to be 1.25 for our analysis.

As seen from eq 13a, one can relate the supersaturation S with the induction time t_{ind}. So, to estimate the interfacial tension γ using Fisher's droplet model, one can take the ratio of any of the two induction times such that

$$\frac{t_{ind(i)}}{t_{ind(j)}} = \frac{C \exp\left(\frac{\Delta G * (S_i, \gamma)}{kT}\right)}{C \exp\left(\frac{\Delta G * (S_j, \gamma)}{kT}\right)} \tag{15a}$$

or

$$kT \ln\left(\frac{t_{ind(i)}}{t_{ind(j)}}\right) = \Delta G^*(S_i, \gamma) - \Delta G^*(S_j, \gamma) \tag{15b}$$

Plotting both sides of the above equation versus γ, eq 15b can be solved graphically to yield the value of γ for our critical size NPSC. After solving eq 15b for different volume fractions and scaling the value of γ with the lattice constant (potential minima), we find the value of γ to be $\gamma = 1.5 \pm 0.2 kT/\sigma^2$. This value of γ compares well with the one calculated earlier from the CNT applied to our simulation results. The critical size calculated from this model is compared with the one calculated based on the CNT, as shown in Table 1. We can see that for a given supersaturation S, the critical size of the cluster N^* is only slightly bigger for the Fisher model in comparison to the CNT. Thus, we conclude that the introduction of the logarithmic term to the CNT does not have a strong effect on the calculation of either γ or N^*.

III.E. Crystalline Nature of the Nucleating Cluster. To characterize the crystalline structure of the nucleating NPSC, we analyze the growing cluster by using the local bond order parameters first introduced by Steinhardt et al.[42] Local bond order parameters are used for the accurate identification of the crystalline structure of clusters[35] and are obtained from an algorithm that is based on spherical harmonics:

$$q_{lm}(i) = \frac{1}{N_b(i)} \sum_{j=1}^{N_b(i)} Y_{lm}(r_{ij}) \tag{16}$$

where $N_b(i)$ denotes the number of nearest neighbors of particle i, l is an integer parameter, $Y_{lm}(r_{ij})$ are the spherical harmonics, and r_{ij} is the unit vector indicating the direction of the bond between particle i and its neighboring particle j. On the basis of these complex vectors, we can calculate the local bond order parameters as

$$q_l(i) \equiv \left[\frac{4\pi}{2l+1} \sum_{m=-l}^{l} |q_{lm}(i)|^2 \right]^{1/2} \tag{17}$$

and

$$\hat{w}_l(i) \equiv w_l(i) / \left[\sum_{m=-l}^{l} |q_{lm}(i)|^2 \right]^{3/2} \tag{18}$$

where $w_l(i)$ is given by

$$w_l(i) = \sum_{\substack{m_1, m_2, m_3 \\ m_1+m_2+m_3=0}} \begin{pmatrix} l & l & l \\ m_1 & m_2 & m_3 \end{pmatrix} \times q_{lm_1}(i) q_{lm_2}(i) q_{lm_3}(i) \tag{19}$$

The terms in the brackets of eq 19 represent the Wigner 3-j symbols.

On the basis of the coherent (representing the *solid-like* behavior) or incoherent addition (representing the *liquid-like* behavior) of the vectors in eq 16, we can identify different crystalline structures in our nucleating NPSCs using these bond order parameters.[43,44] For a pure crystalline structure, these bond order parameters will give one sharp peak at some parameter value. A more useful analysis of the crystal nature of the growing nucleus can be done by using two-dimensional plots of two different bond orientational order parameters.[45] As the growing nucleus will have many defects, we would like to compare it with various pure crystal lattices (fcc, bcc, and hexagonal close-packed (hcp)) with artificially induced spreads in the lattice constants. This spread is created by randomly displacing the particles in the specific pure crystals about their lattice points. The random displacement of the particles varies differently in different regions of the crystals, indicating the different levels of distortions created by the thermal vibrations of the particles in the crystal about their lattice sites. The particles in the *core* (i.e., particles within a distance of R_g from the center) of the cluster are assumed to be less thermally effected, so we have created different shells in the crystals with the particles on the lattice sites of each shell having different random displacement. The details of the random displacement in the shells are given in Table 2.

Table 2. A Table of the Random Variations in the Lattice Sites at Different Shells in the hcp, bcc, fcc and Ich Crystal Lattices

| | variation for hcp, bcc, and fcc in comparison with c12 cluster | | | |
shell	hcp	bcc	fcc	Ich
shell 1< R_g	2%	2%	2%	2%
R_g < shell 2 < R_p	4%	4%	4%	4%
R_p < shell 3	10%	10%	10%	10%

Figure 11a shows the q_4–q_6 surface plot of the nucleating NPSC. For comparison, Figure 11b,c shows the surface plots of
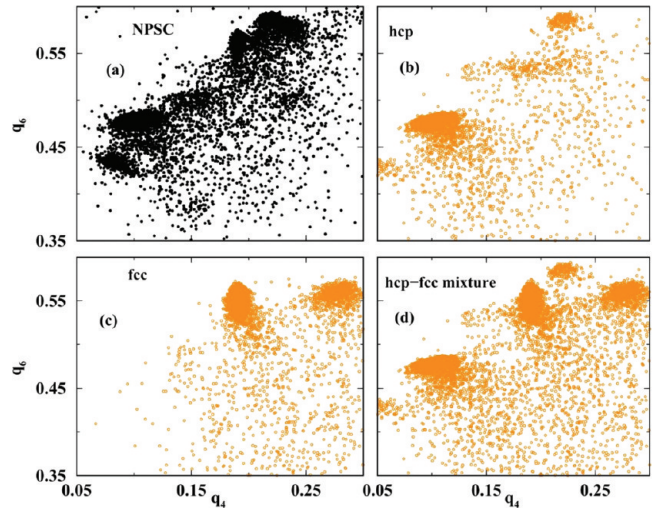

Figure 11. (a) A q_4–q_6 surface plot of the late time nucleating NPSC with a size of $N = 10147$. In panels b and c, surface plots of hcp and fcc randomly distorted crystal structures are shown, respectively. Each crystalline structure has its distinct "islands" on the surface, but a mixture of these two structures, as shown in panel d, indicates that some regions of the nucleating NPSC in this surface plot are strongly dominated by the hcp structure, while in other regions, the NPSC appears to show the strong signatures of the fcc structure.

randomly distorted hcp and fcc clusters, respectively. Each of the crystalline structures compares favorably with some of the isolated patchy regions on the NPSC surface plot. For better comparison, we compared the nucleating NPSC with the mixture of both structures shown in Figure 11d. From Figure 11d, it can be seen that the surface plot of the mixture of both crystalline structures compares well to that of the NPSC in 11a, where the dense regions on the surface indicate the existence of crystalline structures, and the dispersed and scattered data points on the surface are a sign of the appearance of a liquid-like structure in the cluster. We note that these scattered, liquid-like data points always appear in our randomly distorted crystalline structures whenever a distortion of more than 10% is created in the structures (similar to the Lindemann's criterion of melting[46]). It is clear from Figure 11d that the nucleating NPSC compares remarkably well to a randomly displaced 50–50 fcc/hcp mixture.

We also compared the structure of our NPSC with the randomly displaced icosahedral (Ich) crystal (particle position in the crystal being displaced as mentioned in Table 2). Even though pure Ich has a distinct structure and can be easily differentiated from the other close-packed structures such as hcp and fcc, the randomly distorted structure of Ich shows a
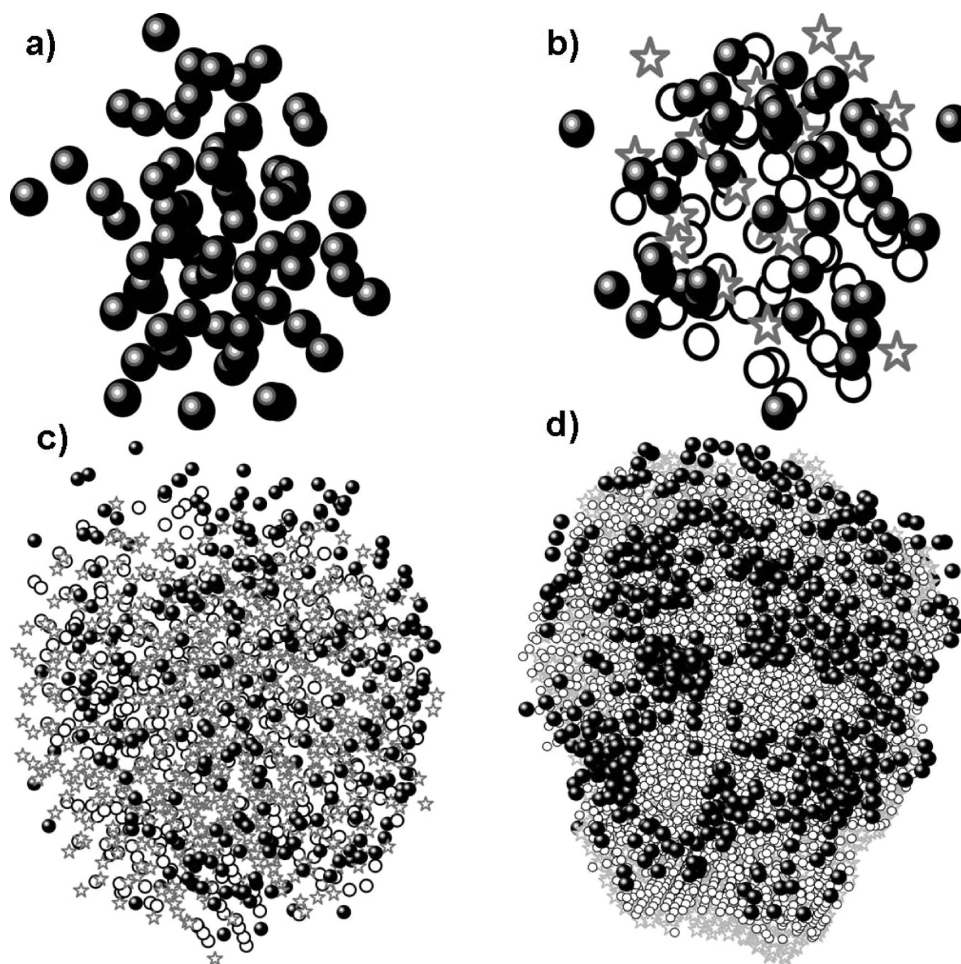
Figure 12. The morphology of the nucleating NPSC in the C12 system showing the presence of liquid structure (●) and different crystalline structures (i.e., fcc (open circles) and hcp (star-shaped)) at (a) $t = 3000$ ($N = 147$), (b) $t = 5000$ ($N = 1296$), (c) $t = 10\,000$ ($N = 5346$), and (d) $t = 40\,000$ ($N = 10147$).

very similar q_4-q_6 surface plot when compared to that of an equal mixture of fcc and hcp. Thus, one can equally conclude that the crystalline structure of the NPSC is similar to the randomly distorted Ich structure.

To further analyze the details of the NPSC morphology and to differentiate between the liquid-like and solid-like particles in the NPSC, we use the scalar product definition of the vector q_6 for the ith particle with the neighboring j particles given by

$$C_{ij} = q_6(i) \cdot q_6(j) = \sum_{m=-6}^{6} q_{6m} q_{6m}^* \tag{20}$$

This vector product between the neighboring particles helps to distinguish between the solid-like and liquid-like particles in the whole cluster. First, we define the *connected* neighbors. Two neighbors are considered to be connected if the above-mentioned correlation function C_{ij} is greater than some threshold value. In the literature, different threshold values of C_{ij} have been used for this purpose. For example, Mendez-Villuendas and Bowles[47] used a threshold value of 0.65, while ten Wolde et al.[44] used a threshold value of 0.5. We did not see any substantial differences in our results whether we use 0.5 or 0.65 as the threshold value. For a distinction between solid-like and liquid-like particles, one can set another threshold value for the number of connections. Following ref 43, any particle that has more than seven connections is considered solid-like;

particles with less than or equal to seven connections are considered as liquid-like.

Once the solid-like or liquid-like behavior of the particles is determined, we further assign the crystalline identity to each solid-like particle i. The method to distinguish the crystalline structure of the solid-like particles is described in ref 48 and is based on the values of $q_4(i)$ and $\hat{w}_4(i)$. According to their definition, if $\hat{w}_4(i) \leq 0$ and $q_4(i) > 0.15$, then the structure of the ith solid-like particle is considered an fcc structure, and if $q_4(i) \leq 0.15$ and $\hat{w}_4(i) > 0$, then the structure is considered hcp. So, on the basis of the above-mentioned definition for the identification of the crystalline structure, we looked at the morphology of the nucleating NPSC at four different times of the growing NPSC in our simulation. The morphology is shown in Figure 12. It can be seen in Figure 12a that at initial times, the particles in the nucleating NPSC have a liquid-like structure, and all different crystalline structures start to appear simultaneously in the NPSC once it achieves a certain size (around 150 particles in this case). As the NPSC grows, the core becomes more crystalline, whereas the surface of the NPSC is more liquid-like, as shown in Figure 12b−d.

From this analysis, it seems clear that the formation of a stable nucleating NPSC is a two-step process. The nucleating embryo is initially liquid-like, and then in the second step, fcc/hcp crystalline structure starts to evolve. Ultimately, different layers of crystalline structure are formed, while the surface of

the nucleating NPSC is always dominated by the liquid-like particles. Similar observation was found by van Meel et al. during their study of the Lennard-Jones system below triple point.[49]

Figure 13 shows the fractional composition of different crystalline structures in the nucleating NPSC as a function of
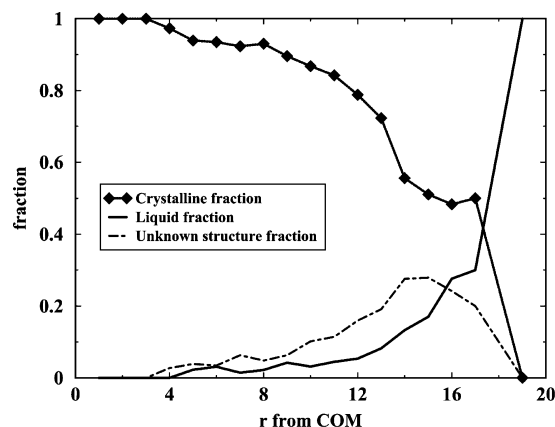

Figure 13. The structure of a nucleating NPSC with N = 5016 at different times during nucleation as a function of the distance "r" (in the units of the diameter of the NP) from the COM for the C12 system. The solid line is indicative of the liquidlike fractional composition, whereas the broken line represents the fraction of the "unknown" structures, i.e., when the structure of the particles does not fit into the defined limits of bond-order parameter values for a given crystalline structure, as mentioned in ref 40. The crystalline structure is the line with symbols. It can be seen that the surface of the cluster always remains liquid-like, whereas the core is mostly close-packed.

the distance from the center of mass (COM). We observe again that the cluster is dominantly liquid-like at early times, but as the cluster grows further, crystalline structures start appearing at the core while the surface of the cluster is always dominated by the liquid-like particles.

IV. CONCLUSIONS

In summary, we have used an effective pair potential between two ligated 5 nm gold nanoparticles in a Brownian dynamics simulation to study nucleation of NPSCs from a temperature quenched NP solution. Both the kinetics and morphology of the NPSCs were studied. Analysis of a prenucleation induction period with classical nucleation theory yielded a supercluster interfacial tension that compares reasonably well with other theory and experimental measurements. We observed that most of the smaller sized prenucleating NPSCs have noncompact morphology, whereas the larger sized NPSCs are compact, and the growth of the nucleating cluster is dominated by the addition/subtraction of monomers as postulated by CNT. An unexpected and surprising observation was that the prenucleation cluster size can occasionally range greater than the critical size in the prenucleation regime without nucleation occurring. Only when a cluster with low enough energy occurs will nucleation ensue. Furthermore, our analysis of the crystalline structure of the nucleating cluster based on the bond orientational order parameter suggests that the formation of the stable nucleating cluster is a two-step process. Initially, a stable liquid-like structure is formed leading to the formation of different crystalline structures growing in the core of the cluster.

We take this opportunity to compare our simulation results with several other experiments. For example, Abécassis et al.[10] studied the formation of an NPSC by in situ SAXS. They observe a very small induction time (about a few seconds). In our simulations, however, we quench the NP monomer system starting from different initial volume fractions (keeping the temperarure constant), and hence the induction time varies as the volume fraction changes, as shown in Figure 4. Also, one should be careful in comparing equilibrium volume fractions directly with our simulations: the equilibrium volume fraction f_e, in our case, is that of the monomers left in the system, whereas the equilibrium volume fraction in the work of Abécassis et al.[10] (i.e., ϕ_{SL}) is the gold volume fraction in the SL (superlattice). Abécassis et al. also provided an experimental structure factor of the NPSC, and they did not observe any evidence of a first liquid stage. This is not surprising when one notes that in the experimental system of ref 10, the nucleating cluster when first observed has about 1000 particles in it, which would be considered a stable size cluster in our simulations with well-defined cryatalline order developed.

We further note that recent papers by Pileni's group[10] use a slight variation of our model proposed in ref 16 and conclude that supracrystal nucleation is mainly driven by solvent-mediated interactions and not solely by the van der Waals interactions among the nanoparticles.

Our results should promote further experimental studies of NPSC nucleation. Because of the large size of the nanoparticles, this is an experimentally accessible system, and both static and dynamic light-scattering studies of prenucleating clusters would shed light on the age-old problem of atomic and molecular system nucleation.

■ AUTHOR INFORMATION

Notes

The authors declare no competing financial interest.

■ REFERENCES

(1) Sardar, R.; Funston, A. M.; Mulvaney, P.; Murray, R. W. *Langmuir* **2009**, *25*, 13840−13851.
(2) Parsad, B. L. V.; Sorensen, C. M.; Klabunde, K. J. *Chem. Soc. Rev.* **2008**, *37*, 1871−1883.
(3) Klabunde, K. J. *Nanoscale Materials in Chemistry*; Wiley Interscience: New York, 2001.
(4) Murray, C. B.; Kagan, C. R.; Bawendi, M. G. *Annu. Rev. Mater. Sci.* **2000**, *30*, 545−610.
(5) Lin, X. M.; Parthasarathy, R.; Jaeger, H. M. Self-Assembly and Physical Properties of Nanocrystal Arrays. *Dekker Encyclopedia of Nanoscience and Nanotechnology*, 2nd ed.; Dekker: New York, 2009.
(6) Murray, C. B.; Kagan, C. R.; Bawendi, M. G. *Science* **1995**, *270*, 1335−1338.
(7) Bentzon, M. D.; Wonterghem, J. V.; Morup, S.; Tholen. *Philos. Mag.* **1989**, *60*, 169−178.
(8) Laird, B. B. *J. Chem. Phys.* **2001**, *115*, 2887.
(9) Yan, H.; Cingarapu, S.; Klabunde, K. J.; Chakrabarti, A.; Sorensen, C. M. *Phys. Rev. Lett.* **2009**, *102*, 095501.
(10) Abecassis, B.; Testard, F.; Spalla, O. *Phys. Rev. Lett.* **2008**, *100*, 115504.
(11) Goubet, N.; Richardi, J.; Albouy, P.-A.; Pileni, M.-P. *Adv. Funct. Mater.* **2011**, *21*, 2693−2704.

(12) Salzemann, C.; Zhai, W.; Goubet, N.; Pileni, M. P. *J. Phys. Chem. Lett.* **2009**, *1*, 149−154.

(13) Kovalenko, M. V.; Talapin, D. V.; Loi, M. A.; Cordella, F.; Hesser, G.; Bodnarchuk, M. I.; Heiss, W. *Angew. Chem., Int. Ed* **2008**, *47*, 3029−3033.

(14) Bodnarchuk, M. I.; Li, L.; Fok, F.; Nachtergaele, S.; Ismagilov, R. F.; Talapin, D. V. *J. Am. Chem. Soc.* **2011**, *133*, 8956−8960.

(15) Vekilov, P., J. *Cryst. Growth* **2005**, *275*, 65−76.

(16) Erdemir, D.; Lee, A. Y.; Myerson, A. S. *Acc. Chem. Res.* **2009**, *42*, 621−629.

(17) ten Wolde, P. R.; Frenkel, D. *Science* **1997**, *277*, 1975.

(18) Gasser, U.; Weeks, E. R.; Schofield, A.; Pusey, P. N.; Weitz, D. A. *Science* **2001**, *292*, 258.

(19) Sloutskin, E. *Bull. Am. Phys. Soc., March Meeting* **2010**, 514.

(20) Khan, S. J.; Pierce, F.; Sorensen, C. M.; Chakrabarti, A. *Langmuir* **2009**, *25* (24), 13861−13868.

(21) Ohara, P. C.; Leff, D. V.; Heaath, J, R.; Gelbart, W. M. *J. Phys. Chem.* **1995**, *75*, 3466−3469.

(22) Smitham, J. B.; Evans, R.; Napper, D. H *J. Chem. Soc., Faraday Trans. 1* **1975**, *71*, 285−297.

(23) Evans, R.; Smitham, J. B.; Napper, D. H *Colloid Polym. Sci.* **1977**, *255*, 161−167.

(24) Abraham, F. F. *Homogeneous Nucleation Theory*; Academic Press: New York and London, 1974.

(25) Debenedetti, P. G. *Metastable Liquids: Concepts and Principles*; Princeton University Press: Princeton, NJ, 1996.

(26) The minimum separation of the particles in the nucleating cluster coincides with the minima of total interaction potential between the nanoparticles, which is 1.33 for the case of C12. Thus, we considered the effective volume of the nucleating cluster as where = 1.33. In addition, the separation distance between two particles is slightly different in the condensed phase, which we have ignored in computing.

(27) Kashchiev, D. *Nucleation: Basic Theory with Applications*; Butterworth-Heiemann: Oxford, U.K., 2000.

(28) Mullin, J. W. *Crystallization*; Butterworth: Oxford, U.K., 1972.

(29) Cerda, J. J.; Sintes, T.; Holm, C.; Sorensen, C. M.; Chakrabarti, A. *Phys. Rev. E* **2008**, *78*, 031403.

(30) Kulkarni, A. M.; Zukoski, C. F. *Langmuir* **2002**, *18*, 3090−3099.

(31) Alexander, S.; McTague, J. P. *Phys. Rev. Lett.* **1978**, *41*, 702−705.

(32) ten Wolde, P. R.; et al. *Phys. Rev. Lett.* **1995**, *75*, 2714−2717.

(33) Xu, S.; Zhou, H.; Sun, Z.; Xie, J. *Phys. Rev. E* **2010**, *82*, 010401.

(34) Zhou, H.; Xu, S; Sun, Z.; Du, X.; Liu, L. *Langmuir* **2011**, *27*, 7439−7445.

(35) Lothe, J.; Pound, G. M. *J. Chem. Phys.* **1962**, *36*, 2080.

(36) Fisher, M. E. *Physics* **1967**, *3*, 255.

(37) Egginton, A.; Kiang, C. S.; Stauffer, D.; Walker, G. H. *Phys. Rev. Lett.* **1971**, *26*, 820.

(38) Kiang, C. S.; Stauffer, D.; G., H.; Walker, G. H.; Puri, O. P.; Wise, J. D. Jr.; Patterson, E. M. *J. Atmos. Sci.* **1971**, *28*, 1222.

(39) Racz, Z.; Vicsek, T. *Phys. Rev. Lett.* **1983**, *51*, 2382.

(40) Perini, A.; Jacucci, G.; Martin, G. *Phys. Rev. B* **1984**, *29*, 5.

(41) Lowe, M. J.; Wallace, D. J. *J. Phys. A* **1980**, *13*, L381.

(42) Steinhardt, P. J.; Nelson, D. R.; Ronchetti, M. *Phys. Rev. B* **1983**, *28*, 784.

(43) ten Wolde, P. R.; et al. *Faraday Discuss.* **1996**, *104*, 93−110.

(44) ten Wolde, P. R.; et al. *J. Chem. Phys.* **1996**, *104* (24), 9932.

(45) Lechner, W.; Dellago, C. *J. Chem. Phys.* **2008**, *129*, 114707.

(46) Kaneyoshi, T. *Introduction to Surface Magnetism*; CRC Press: Boca Raton, FL, 1990.

(47) Mendez-Villuendas, E.; Bowles, R. K. *Phys. Rev. Lett.* **2007**, *98*, 185503.

(48) Desgranges, C.; Delhommelle, J. *Phys. Rev. B* **2008**, *77*, 054201.

(49) van Meel, J. A.; et al. *J. Chem. Phys.* **2008**, *129*, 204505.